Processing of continuous data at Apache Forties for seismic interferometry

Jason P. Chang

ABSTRACT

I process continuous data from the Apache Forties data set for use in studies relating to passive seismic imaging. Spectrograms from multiple nodes indicate the presence of strong, naturally-occurring seismic energy at frequencies below 1 Hz, as well as the presence of seismic energy above 4 Hz that originates from the oil platform. After ignoring times of active seismic shooting, I perform passive seismic interferometry on over 2 days of hydrophone and vertical geophone data. For frequencies between 1.00 and 1.25 Hz, there are indications of Scholte-wave energy. However, the expected wavelengths (approximately 150 m/s) at these frequencies are likely comparable to the aperture of the array (approximately 400 m), which compromises the reliability of the arrivals. For frequencies between 3.00 and 7.00 Hz, there are no clear indications of interface waves. Asymmetry of seismic energy in the virtual source gathers suggests that platform vibrations dominate the ambient noise field at high frequencies.

INTRODUCTION

Passive seismic interferometry suggests that cross-correlating simultaneous recordings of ambient noise at two receivers can estimate the Green's function between them (Lobkis and Weaver, 2001; Wapenaar, 2004; Snieder, 2004). These estimated Green's functions are typically dominated by low-frequency interface waves, which have in turn been used for tomographic imaging at primarily the regional and continental scales (e.g., Shapiro et al., 2005; Sabra et al., 2005; Lin et al., 2007). Given the success of these studies, efforts have shifted to applying this technique to recordings from exploration-scale seismic arrays. Focusing on frequencies in the microseism band (between 0.1 and 2.0 Hz), de Ridder and Dellinger (2011) and Mordret et al. (2013) processed ocean-bottom cable recordings of ambient noise to recover interstation Scholte waves at the Valhall oil field. Energy in the microseism band is generated by the natural interaction of water waves in seas and oceans. It is different from microseismic energy, which originates from small earthquakes typically induced by production and drilling activity. The microseism waves are used to tomographically image the reservoir overburden. Additionally, the dense node spacing associated with exploration-scale arrays (approximately 100 m) allows for seismic interferometry to be applied to ambient noise at higher frequencies. For instance, Mordret et al. (2013)

showed that platform energy dominates the ambient noise field at frequencies above 2 Hz at the Valhall field and used that energy to estimate shear-wave velocity along a 2D line.

In this study, we apply the seismic interferometry technique to recordings of ambient noise from a small array of ocean-bottom nodes (OBNs) in the North Sea. Although this is four-component data, I only examine recordings from the hydrophone and vertical-component geophone. First, I provide an overview of the OBN array and its continuous recordings. Second, I compute spectrograms to examine how the ambient seismic noise field changes over time. Finally, I cross-correlate recordings to estimate interstation Green's functions over two frequency ranges. For the frequency range focused on the microseism band, there are indications of coherent seismic events. However, they are likely not reliable enough for use in a tomographic procedure. For frequencies between 3.00 and 7.00 Hz, there are no clear seismic events. However, the asymmetry of energy in the correlations suggests that the platform dominates the ambient noise field at these frequencies.

CONTINUOUS RECORDINGS FROM FORTIES

The Forties data set, provided to SEP by the Apache Corporation, consists of three groups of OBNs centered at three different platforms in the North Sea. The nodes were deployed as part of an active seismic survey aimed at imaging shallow gas pockets that could pose potential drilling hazards. Unlike some other reservoirs in the North Sea, the Forties reservoir is not easily compacted and is unlikely to generate significant activity of this type. The nodes were continuously recording, and because active seismic shooting had to be suspended for a couple of days due to rough weather conditions, there is enough ambient noise data to attempt to perform seismic interferometry. Furthermore, stormy weather conditions tend to increase the upper limit of the microseism energy (de Ridder and Dellinger, 2011), which is ideal in this case given the limited aperture of the OBN clusters.

For this study, we focus on hydrophone and vertical geophone components of one of the three groups of OBNs. Referred to as Bravo, this cluster of OBNs consists of 52 4-component nodes arranged in a hexagonal shape around a platform (Figure 1). The average node spacing is 50 m, and the array aperture is approximately 400 m. Each node continuously records for approximately 4 days at 2 ms sampling and is located roughly 120 m below the sea surface. To prepare the recordings for ambient noise processing, I round the start times up to the nearest hour and round the end times to the nearest hour. These times will not be the same for all nodes, as they were not all deployed simultaneously.

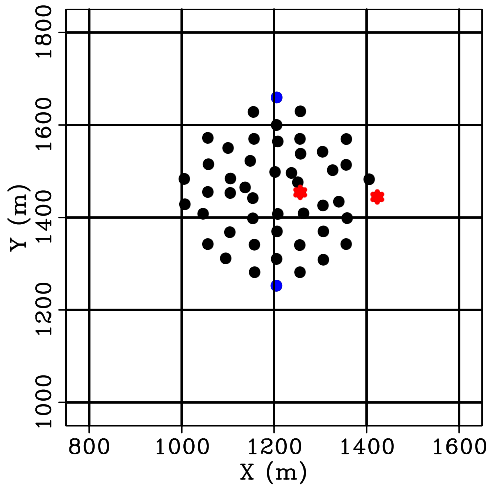

Figure 1: Map of OBNs in the Bravo array. The platform is in the center of the array. Red dots indicate virtual source locations. They are also the nodes at which I compute spectrograms. Blue dots indicate receiver locations for the traces shown later in the study. [**ER**]

SPECTROGRAMS

To investigate the change in frequency content over time in the continuous recordings, I compute spectrograms of the hydrophone and vertical-component geophone at two nodes (indicated by red dots in Figure 1). I divide the recordings into 5-minute time segments with 50% overlap, compute the power spectrum of each segment, then plot them side by side. To enhance important features, I plot the spectrograms on a log scale for frequencies up to 8 Hz.

Figures 2(a) and 2(b) reveal the spectrograms for the hydrophone component at the western and eastern nodes (Figure 1), respectively. Colors in both plots have the same clip. The repeating horizontal patterns at regular frequency intervals on day 110 and days 111.5 to 112.5 indicate periods of active seismic shooting. Of more interest to this study is the clear microseism energy found at frequencies below 1 Hz. As mentioned in the previous section, active seismic shooting was suspended due to rough weather conditions. This is visible starting around day 110, where the microseism energy increases dramatically right before active shooting is halted. The microseism energy remains strong for a couple of days before active shooting resumes and appears to be nearly the same strength at both node locations, which is expected for low-frequency energy in a small array. At frequencies above 2 Hz, there tends to be more energy when the node is closer to the platform. Similar patterns are observed in the spectrograms of the vertical-component geophones (Figures 2(c) and 2(d), corresponding to the western and eastern nodes, respectively). As before, the microseism energy at both node locations is nearly the same strength. It is also apparent that there is more energy at higher frequencies when the node is near the platform than when the node is further away from the platform. Therefore, it appears that the energy source is well-distributed in space at low frequencies and localized at the platform at higher frequencies.

In all the spectrograms, there is a streak of energy at 2 Hz that persists for roughly 1 day, starting at day 110.5. The cause of high energy at this specific frequency

is unknown. It is observed in all spectrograms, suggesting it is due to a physical phenomenon, perhaps related to the platform, and not due to instrument malfunction. Overall, there appears to be significant microseism and platform energy in the data, which is promising for passive seismic interferometry.

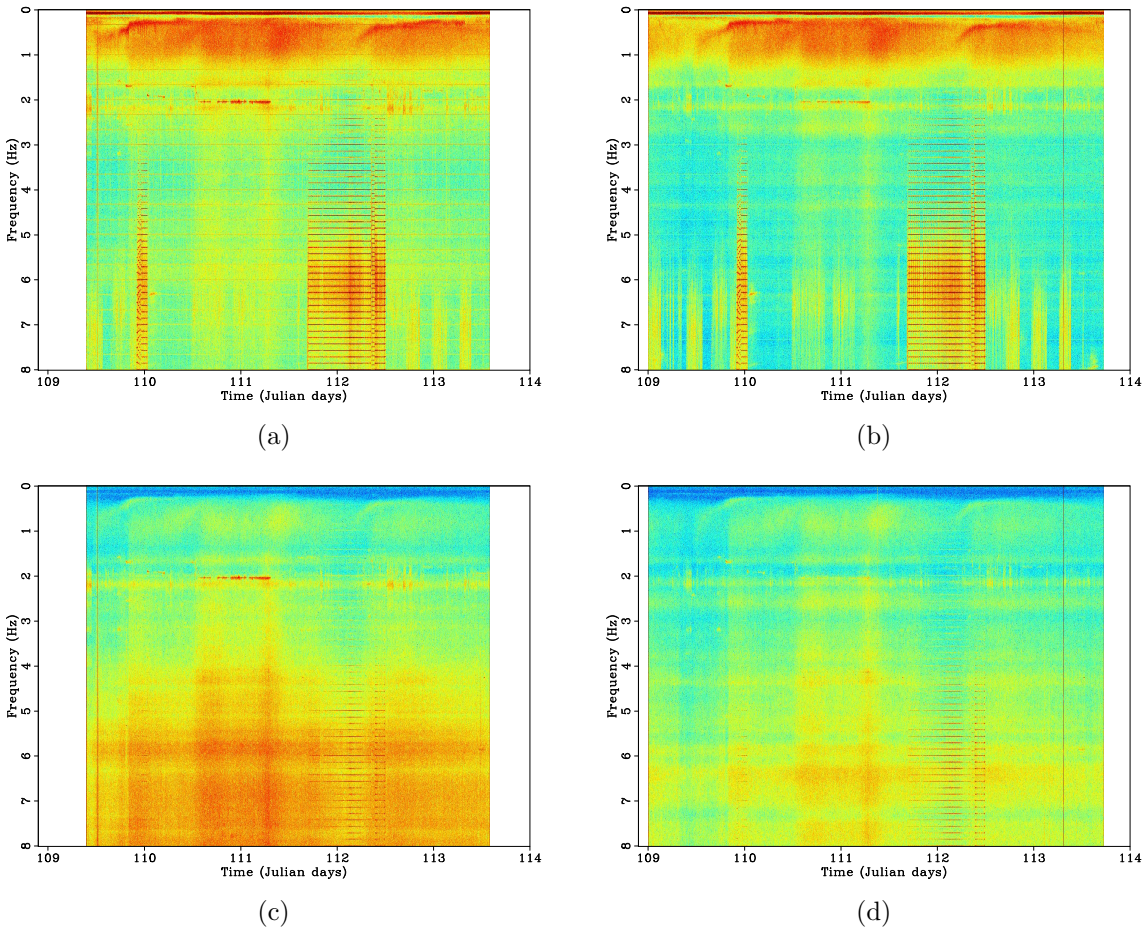

Figure 2: Spectrograms computed at two nodes (indicated by red dots in Figure 1). Hydrophone component for (a) western node and (b) eastern node. Vertical component for (c) western node and (d) eastern node. The western node is close to the platform. Warmer colors indicate higher power. Colors in all plots have the same clip. [**ER**]

SEISMIC INTERFEROMETRY

To perform seismic interferometry on ambient noise, the data records must be synchronized in time. Therefore, all node recordings are truncated to the latest start time and the earliest end time amongst the group of nodes. Because three of the nodes had anomalously short recording periods, I work with 49 out of the 52 possible nodes in Bravo. I then divide the remaining continuous recordings into 2-hour time

windows with 50% overlap for two reasons. First, cross-correlating shorter, overlapping records and then summing them leads to more rapid convergence than when cross-correlating the full recordings themselves (Seats et al., 2012). This is particularly advantageous in this case, where there is only about 4 days of data. Second, dividing the long recordings into shorter ones makes it easier to ignore times when active seismic shooting is occurring. If the maximum absolute value of a trace (bandpassed for frequencies between 4 and 50 Hz) is above a certain threshold, all traces for that time segment are avoided when summing the correlation results. I end up using 52 out of the 74 possible 2-hour segments, leading to over 2 days of ambient noise data.

Passive seismic interferometry is performed by cross-correlating the recordings of ambient seismic noise at two receivers. Under ideal conditions, the result is an estimate of the Green's function between the two receivers, and it is typically dominated by interface waves because they are the strongest wave modes in ambient seismic noise (Wapenaar et al., 2010). Here, I apply a correlation procedure adapted from Bensen et al. (2007). To compensate for expected variations in source amplitude over time and to broaden the bandwidth of the correlation result without changing the phase information, I perform spectral whitening on the traces prior to cross-correlation. In the frequency domain, the procedure is expressed as:

$$[G(x_B, x_A, \omega) + G^*(x_B, x_A, \omega)] = \left\langle \left(\frac{U(x_B, \omega)}{\{|U(x_B, \omega)|\}} \right) \left(\frac{U^*(x_A, \omega)}{\{|U(x_A, \omega)|\}} \right) \right\rangle, \qquad (1)$$

where G is the Green's function between two receiver locations (x_A, x_B), $U(x, \omega)$ is the spectrum of the wavefield at a given receiver location x, $*$ is the complex conjugate, $\langle \cdot \rangle$ is the time-averaged ensemble, $|\cdot|$ is the magnitude of the spectrum, and $\{\cdot\}$ is a 0.003 Hz running window average used for normalizing the signal. This procedure is equivalent to calculating the cross-coherence between two traces.

By cross-correlating one node with all other nodes, I am able to create a virtual source gather. Here, I create virtual source gathers centered at the two node locations indicated by red dots in Figure 1. For both the hydrophone and vertical-geophone components, I investigate two frequency ranges: 1.00–1.25 Hz (for the microseism energy) and 3.00–7.00 Hz (for the platform energy). Gathers are sorted by distance between the virtual source and receiver. Figure 3 shows the hydrophone component, while Figure 4 shows the vertical geophone component. For the lower frequency range, there are clear coherent events from both virtual source locations that are potentially Scholte waves (Figures 3(a) and 3(c) for the hydrophone; Figures 4(a) and 4(c) for the vertical geophone). However, for the higher frequency range, there appears to be no clear coherent seismic energy (Figures 3(b) and 3(d) for the hydrophone; Figures 4(b) and 4(d) for the vertical geophone). The gathers are asymmetric, though, which indicates an uneven source distribution.

For a closer look at the lower-frequency waveforms, Figure 5 plots the correlation results between the virtual sources and receivers shown by colored dots in Figure 1. I only show the hydrophone component because the vertical geophone component looks

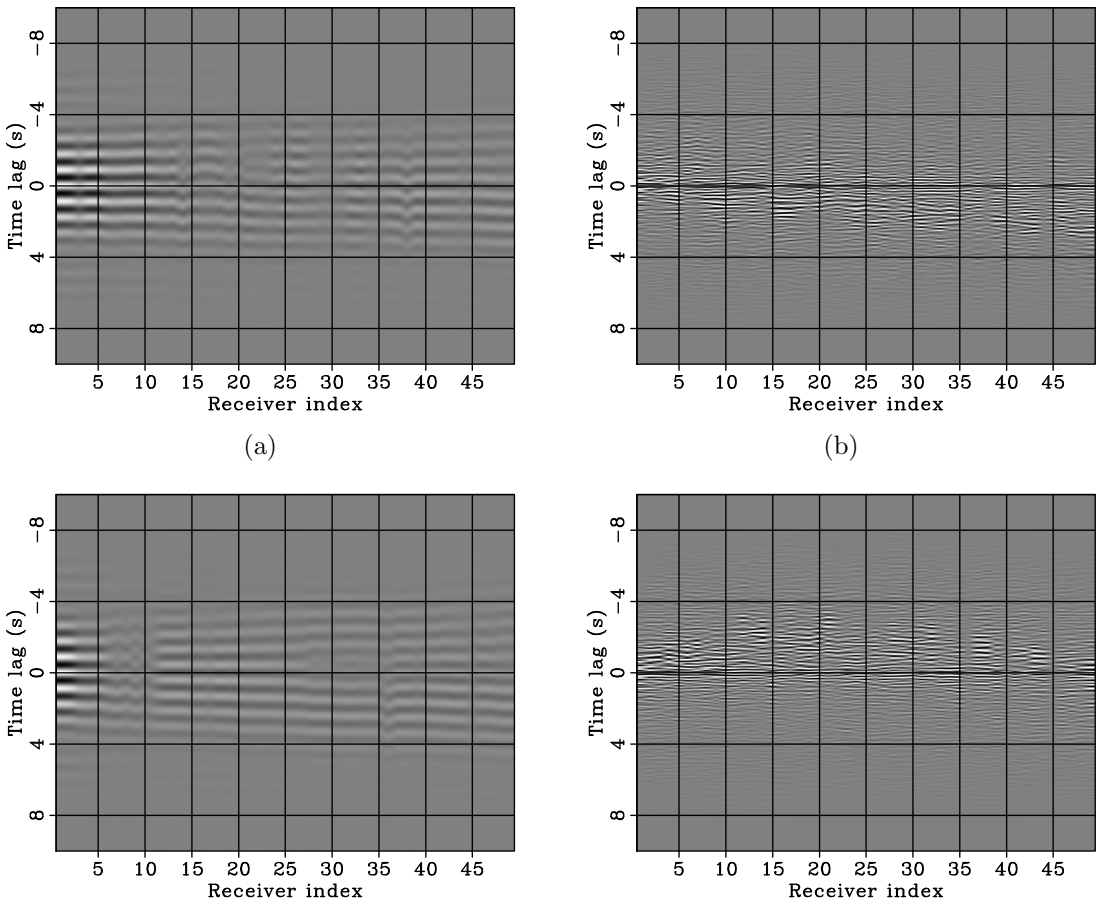

Figure 3: Virtual source gathers of the hydrophone component. Virtual source locations are indicated by red dots in Figure 1. Western source location (near platform): (a) 1.00–1.25 Hz and (b) 3.00–7.00 Hz. Eastern source location: (c) 1.00–1.25 Hz and (d) 3.00–7.00 Hz. [**CR**]

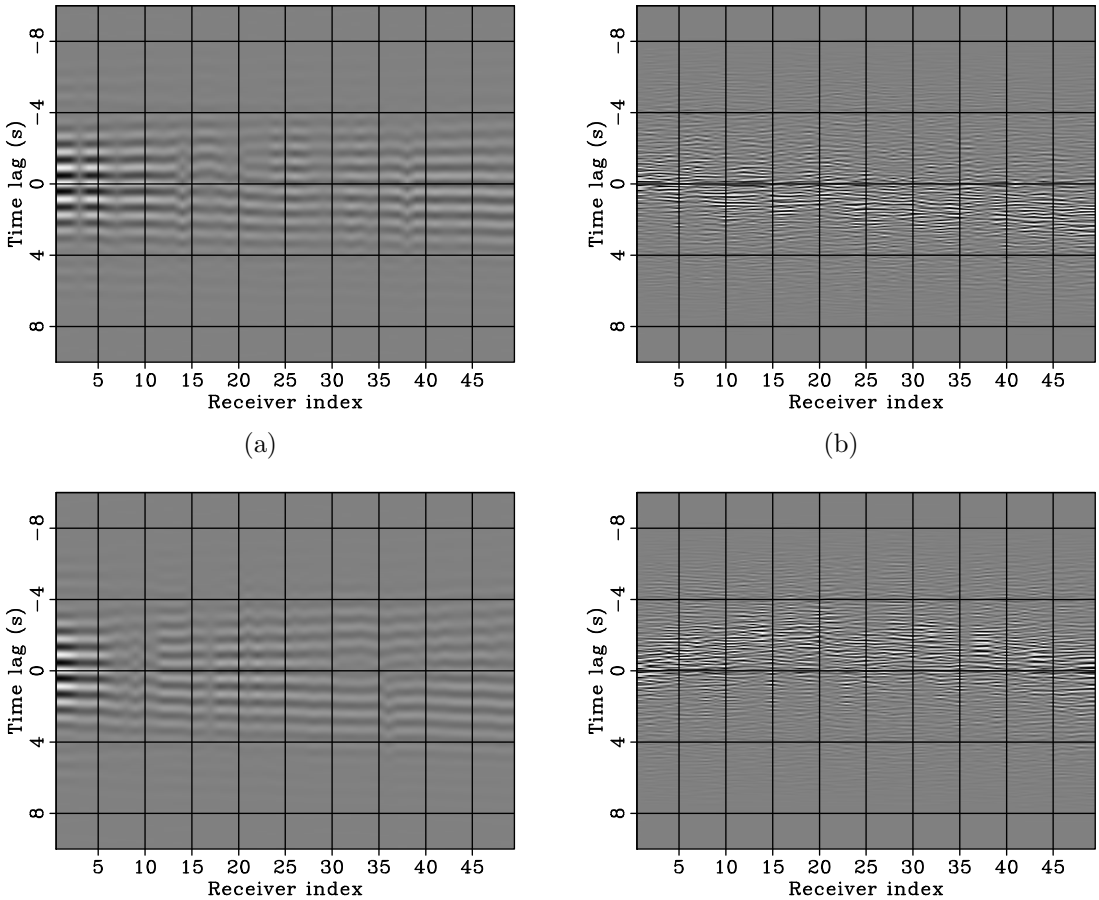

Figure 4: Virtual source gathers of the vertical geophone component. Virtual source locations are indicated by red dots in Figure 1. Western source location (near platform): (a) 1.00–1.25 Hz and (b) 3.00–7.00 Hz. Eastern source location: (c) 1.00–1.25 Hz and (d) 3.00–7.00 Hz. [**CR**]

very similar. When the distance between the virtual source and receiver is larger (Figures 5(c) and 5(d)), apparent Scholte-wave arrivals at negative and positive time lags are clear. When the distance between the virtual source and receiver is smaller (Figures 5(a) and 5(b)), then there appears to only be one Scholte-wave arrival near zero time lag.

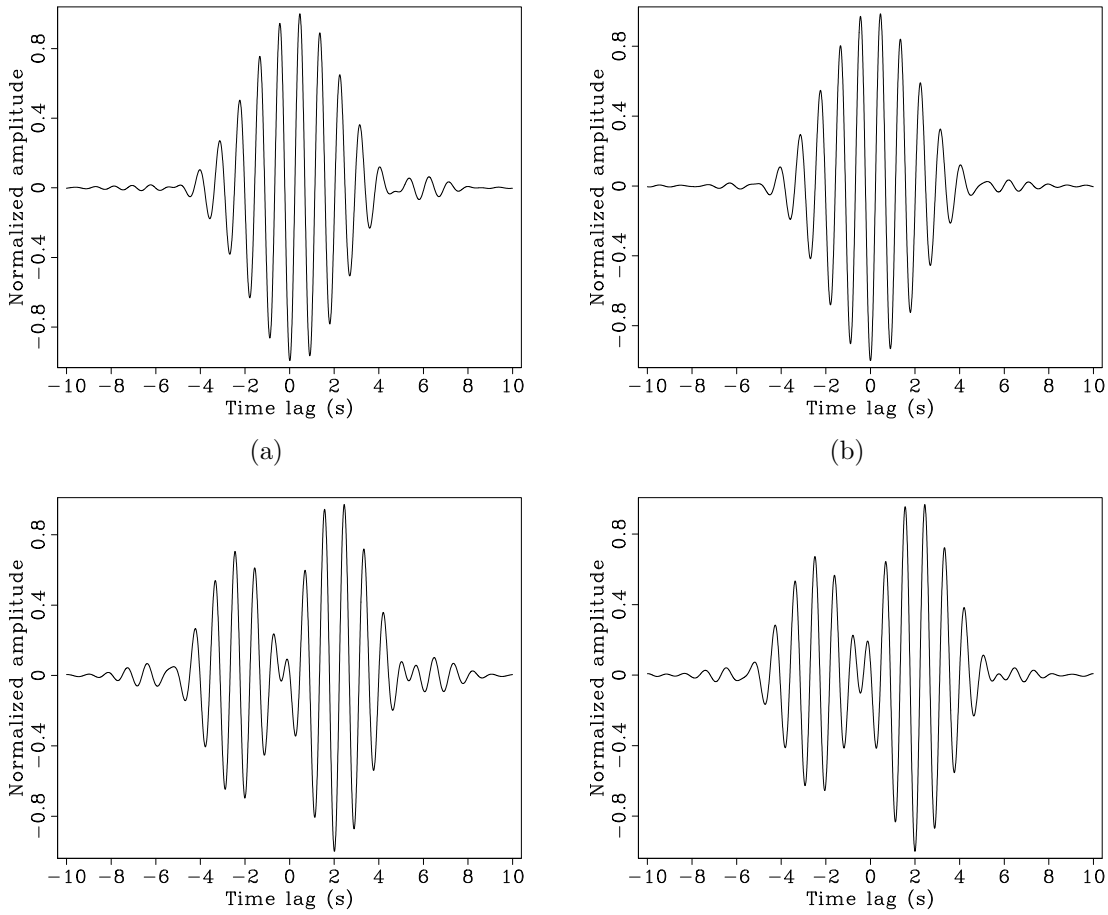

Figure 5: Correlations of hydrophone data at 1.00–1.25 Hz from virtual sources and receivers shown in Figure 1. (a) Between the western virtual source and northern receiver. (b) Between the western virtual source and southern receiver. (c) Between the eastern virtual source and northern receiver. (d) Between the eastern virtual source and southern receiver. The western virtual source is near the center of the array and is thus closer to the receiver locations. [**CR**]

DISCUSSION

Results of passive seismic interferometry indicate the shortcomings of the array when attempting to extract Scholte waves from ambient noise in the microseism band. Given the investigation frequencies and general North Sea Scholte-wave phase veloc-

ities between 200 and 400 m/s at those frequencies (de Ridder and Dellinger, 2011; Mordret et al., 2013), it is very likely that the wavelengths of the estimated Scholte waves (optimistically around 150 m) are comparable to the aperture of the Bravo array (approximately 400 m). This would violate the far-field approximation for reliable travel times, where the distance between the virtual source and receiver should be at least three times the wavelength (Lin et al., 2008). Thus, while the virtual source gathers appear to show Scholte-wave-related arrivals, their travel times are unlikely to be reliable. This includes not only the correlations between nearby nodes (Figures 5(a) and 5(b)), where there is only one apparent arrival with a travel time near 0 s, but also correlations between more distant nodes (Figures 5(c) and 5(d)). Even though these distant nodes display strong events at both negative and positive time lags, their apparent travel times of 3 s are unrealistic given the station spacings of 300 m and the expected velocities between 200 and 400 m/s seen in other regions of the North Sea.

Ideally, there would be coherent energy at higher frequencies, which would correspond to shorter wavelengths. From the spectrograms, it appears that the oil platform is the dominant source of energy at frequencies higher than the microseism band. From the high-frequency virtual source gathers, there is a clear asymmetry in the correlations that supports this conjecture. Events at negative time lags correspond to energy traveling from the receiver to the virtual source, while positive time lags correspond to energy traveling from the virtual source to the receiver. Energy is found primarily at negative time lags when the virtual source is east of the platform (Figures 3(d) and 4(d)). This is expected, as the majority of the energy travels east toward the virtual source location from the platform. Furthermore, energy appears to arrive at near-zero travel time at far offsets, which is an indication of an active source in the region (Chang et al., 2014). Alternatively, energy is found primarily at positive time lags when the virtual source location is near the platform. Again, this is expected, as the energy is propagating away from the virtual source location (the platform) to the other nodes. Therefore, there is substantial evidence that the platform is the dominant source of energy at high frequencies. Unfortunately, the platform does not seem to be energetic enough to stimulate strong interface waves that can be recovered through standard seismic interferometry given the amount of ambient noise data available.

CONCLUSIONS

The Apache Forties OBN survey provided an opportunity to apply passive seismic interferometry to hydrophone and vertical-geophone data from a small, ocean-bottom array. Spectrograms revealed that the microseism energy is nearly equally energetic across the array, while energy at higher frequencies is dependent on distance from the platform, which is the dominant source of noise at these frequencies. I then applied seismic interferometry to times without active seismic shooting. At frequencies between 1.00 and 1.25 Hz, there appears to be interface-wave-related energy. However,

because the expected wavelength of these waves are comparable to the maximum aperture of the array of 400 m, it is unlikely the travel times associated with these events are reliable. At frequencies between 3.00 and 7.00 Hz, there are no indications of clear interface-wave arrivals. However, the asymmetry in the correlations reaffirm that the platform is the primary source of noise at high frequencies.

Although the ambient noise data at the Forties is not immediately useful for seismic interferometry and ambient noise tomography, it still contains potential for passive fathometry. Rough weather conditions and more violent breaking waves at the sea surface are ideal for the technique, which attempts to create shallow subsurface reflection images by correlating passive up- and down-going energy. Understanding of the noise sources in and around the array is useful for creating filters to dampen horizontally-traveling waves, including interface waves.

ACKNOWLEDGMENTS

The author would like to thank Apache North Sea Limited for access to the data set and permission to publish. The author also thanks Shuki Ronen and Stewart Levin for help processing the data and useful discussions.

REFERENCES

Bensen, G., M. Ritzwoller, M. Barmin, A. Levshin, F. Lin, M. Moschetti, N. Shapiro, and Y. Yang, 2007, Processing seismic ambient noise data to obtain reliable broad-band surface wave dispersion measurements: Geophysical Journal International, **169**, 1239–1260.

Chang, J. P., N. Nakata, R. G. Clapp, B. Biondi, and S. de Ridder, 2014, High-frequency surface and body waves from ambient noise cross-correlations at Long Beach, CA: 84th Annual International Meeting, SEG, Expanded Abstracts, 2235–2239.

de Ridder, S. and J. Dellinger, 2011, Ambient seismic noise eikonal tomography for near-surface imaging at Valhall: The Leading Edge, **30**, 506–512.

Lin, F.-C., M. P. Moschetti, and M. H. Ritzwoller, 2008, Surface wave tomography of the western United States from ambient seismic noise: Rayleigh and Love wave phase velocity maps: Geophysical Journal International, **173**, 281–298.

Lin, F.-C., M. H. Ritzwoller, J. Townend, S. Bannister, and M. K. Savage, 2007, Ambient noise Rayleigh wave tomography of New Zealand: Geophysical Journal International, **170**, 649–666.

Lobkis, O. I. and R. L. Weaver, 2001, On the emergence of the Green's function in the correlations of a diffuse field: The Journal of the Acoustical Society of America, **110**, 3011–3017.

Mordret, A., M. Landès, N. Shapiro, S. Singh, P. Roux, and O. Barkved, 2013, Near-surface study at the Valhall oil field from ambient noise surface wave tomography: Geophysical Journal International, ggt061.

Sabra, K. G., P. Gerstoft, P. Roux, W. Kuperman, and M. C. Fehler, 2005, Extracting time-domain Green's function estimates from ambient seismic noise: Geophysical Research Letters, **32**, L03310.

Seats, K. J., J. F. Lawrence, and G. A. Prieto, 2012, Improved ambient noise correlation functions using Welch's method: Geophysical Journal International, **188**, 513–523.

Shapiro, N. M., M. Campillo, L. Stehly, and M. H. Ritzwoller, 2005, High-resolution surface-wave tomography from ambient seismic noise: Science, **307**, 1615–1618.

Snieder, R., 2004, Extracting the Green's function from the correlation of coda waves: A derivation based on stationary phase: Physical Review E, **69**, 046610.

Wapenaar, K., 2004, Retrieving the elastodynamic Green's function of an arbitrary inhomogeneous medium by cross correlation: Physical Review Letters, **93**, 254301.

Wapenaar, K., D. Draganov, R. Snieder, X. Campman, and A. Verdel, 2010, Tutorial on seismic interferometry: Part 1—Basic principles and applications: Geophysics, **75**, no. 5, 75A195–75A209.